Research Article

Wullapa Wongsinlatam, Jaruwan Thepsiri, Sasiporn Audtarat, Manop Sriuttha and Thananchai Dasri*

Synthesis of ZnO nanoparticles with different morphologies using a microwave-based method and their antimicrobial activity

https://doi.org/10.1515/ntrev-2025-0240
Received May 27, 2025; accepted October 14, 2025;
published online December 4, 2025

Abstract: Zinc oxide nanoparticles (ZnONPs) are versatile nanomaterial that has consistently attracted research attention. This work presents a simple and cost-effective method for synthesizing ZnONPs using a microwave-based method. ZnONPs with different morphologies can be obtained by varying the sodium hydroxide (NaOH) reactant concentration. The synthesized products were morphologically and structurally investigated using field emission scanning electron microscopy (FESEM) and energy dispersive X-ray (EDX) analysis, Fourier transform infrared spectroscopy (FTIR), and X-ray diffractometry (XRD). Additionally, the optical characteristics of the synthesized products were confirmed with UV–vis and Raman spectroscopy. The UV–vis spectra exhibit a prominent absorption band characteristic of ZnO. The FTIR spectra of ZnONPs in the 300–4,000 cm^{-1} range consist of bands corresponding to specific functional groups of biomolecules and metal oxides. The obtained XRD diffraction peaks can be assigned to a hexagonal wurtzite ZnO structure. The FTIR absorption peaks in the 495–850 cm^{-1} range confirm the structure of ZnONPs. According to the antimicrobial testing results, the products show growth inhibition against Gram-positive *Staphylococcus aureus* and *Bacillus subtilis*, as well as Gram-negative *Escherichia coli* and *Klebsiella pneumoniae* bacteria. Therefore, ZnONPs of all morphologies could be applied as antimicrobial agents.

Keywords: microwave method; zinc oxide nanoparticles; different morphologies

***Corresponding author: Thananchai Dasri**, Faculty of Interdisciplinary Studies, Khon Kaen University, Nong Khai Campus, Nong Khai 43000, Thailand, E-mail: thananchai@kku.ac.th
Wullapa Wongsinlatam, Jaruwan Thepsiri, Sasiporn Audtarat and Manop Sriuttha, Faculty of Interdisciplinary Studies, Khon Kaen University, Nong Khai Campus, Nong Khai 43000, Thailand

1 Introduction

Nanostructured metal and metal oxides, like Ag, Au, Cu, Fe_3O_4, TiO_2, CuO, and ZnO, among others, are increasingly the focus of research in material science applications due to their unique properties [1–12]. Their specific properties depend on their morphology, size, concentration, surrounding medium, and structure, which differ significantly from bulk materials [13]. Due to the need for specific applications, many distinctive forms of nanoparticles (NPs), such as pure NPs, core–shell NPs, multilayered core–shell NPs, and polymer-coated metal oxide NPs, among others, have been reported [9, 14, 15]. Among the metal oxides used as benchmark materials, zinc oxide (ZnO) has remarkable ultraviolet (UV) absorbing, optical and optoelectronic properties owing to its wide band gap of 3.37 eV and large exciton binding energy of 60 meV, making it valuable for various commercial applications [16, 17]. Currently, ZnO nanoparticles (ZnONPs) have emerged in sectors like the food industry [18–20], as well as agricultural and environmental fields [17, 21, 22]. ZnONPs are used as inorganic antimicrobial agents in biomedical applications [17, 21, 23–26], catalytic and biological applications [27–29], as well as in cosmetics [24, 30] and optical devices [24, 31–33]. Several ZnONP synthesis methods have been presented in the literature, including chemical co-precipitation, a hydrothermal process, chemical vapor deposition, and a sol–gel process [17, 24]. However, these methods commonly produce toxic by-products. Although the biosynthesis of ZnONPs using plants, algae, yeast, and fungi can reduce the use of hazardous chemicals [17, 24, 34–36], it faces numerous limitations, including raw material selection, reaction conditions, and product quality control. The synthesis time for many biosynthesis methods is long, and the optimum temperature is relatively high, requiring significant energy. Such processes can be harmful to the environment, even when using environmentally acceptable starting ingredients. Syntheses that require less time and fewer harmful chemicals and are easy to scale are also important [30]. Therefore, alternative methods should be considered for the synthesis of ZnONPs.

Microwave synthesis of ZnONPs has emerged as an efficient technique with numerous advantages over chemical and biological methods [37, 38]. Additionally, the main advantage of the microwave method is the significant reduction in overall synthesis process time, which is due to the high heating rate. The application of microwave heating technology in the synthesis of ZnONPs has enabled the development of new synthetic methods with properties such as controllability, reproducibility, short synthesis time, low cost and purity, which are considered environmentally friendly. This research aimed to synthesize ZnONPs using the microwave heating method, considering the synthetic parameters affecting particle morphology, the potential of a simple and rapid synthetic method, and antimicrobial properties. The influence of sodium hydroxide (NaOH) concentration on the morphology of synthesized ZnONPs was investigated. Morphological control directly affects the physicochemical properties and antibacterial efficacy [39–41]. It not only increases the surface area and reactivity of ZnONPs but also plays a key role in regulating their interaction with bacterial cells. Following the formation of ZnONPs and characterization of the synthesized material, antimicrobial activity tests were performed using the ZnONPs. According to the antimicrobial test results, ZnONPs of all morphologies can potentially be applied as antimicrobial agents in various industrial applications.

2 Materials and methods

2.1 Chemicals and instrumentation

Zinc acetate dehydrate was purchased from QRëC (New Zealand). Sodium hydroxide (NaOH) was procured from RCI Labscan, Limited (Thailand). All chemical materials are of analytical grade and utilized without further purification. Pathogenic bacteria, Gram-positive *Staphylococcus aureus* (*S. aureus*) and *Bacillus subtilis* (*B. subtilis*) and Gram-negative *Escherichia coli* (*E. coli*) and *Klebsiella pneumonia* (*K. pneumonia*) were obtained from the Biosafety Laboratory Level 2, Faculty of Interdisciplinary Studies, Khon Kaen University, Nong Khai Campus, Thailand.

2.2 Microwave-assisted synthesis of ZnONPs

Zinc acetate dihydrate (0.149 M) was dissolved in 100 mL of deionized water. Additionally, different concentrations (0.50, 0.72, 1.78, and 2.00 M) of NaOH were dissolved in 30 mL of deionized water. Then, the zinc acetate dihydrate and NaOH solutions were mixed until they were well combined. This mixed solution was then heated in a microwave oven at 800 W for 6 min. After that, the obtained solution was cooled to room temperature. Finally, a solution containing a white precipitate was centrifuged at 6,000 rpm for 3 min, washed several times with deionized water, and dried for 24 h at 60 °C in an oven. Samples prepared with four different NaOH concentrations were evaluated in this work. Samples with NaOH concentrations of 0.50, 0.72, 1.78, and 2.00 M are referred to as ZnO-0.50 M NaOH, ZnO-0.72 M NaOH, ZnO-1.78 M NaOH, and ZnO-2.00 M NaOH, respectively.

2.3 Characterization

The synthesized ZnONPs forms in colloidal solution were verified under UV–vis spectroscopy (Shimadzu UV-1900i, Japan), over a 300–800 nm wavelength range. Field emission scanning electron microscopy (FESEM) (TESCAN, Model MIRA) was operated at a 7 keV accelerating voltage. Energy dispersive X-ray spectroscopy (EDS) was performed to obtain the surface elemental composition of composite materials. Functional groups were investigated through Fourier transform infrared (FTIR) spectroscopy in the wave number range from 400–4,000 cm^{-1}. The crystalline phases of composite materials were investigated using X-ray diffraction (XRD) over the 20°–80° 2θ range. Finally, Raman spectrometry (HORIBA, Model XploRA plus) was employed to clarify the quality and structure of the products in the wave number range between 300 and 700 cm^{-1}.

2.4 Antimicrobial activity tests

The antimicrobial performance of the ZnO-0.50 M NaOH, ZnO-0.72 M NaOH, ZnO-1.78 M NaOH, and ZnO-2.00 M NaOH specimens was tested against Gram-positive *S. aureus* and *B. subtilis*, as well as Gram-negative *E. coli* and *Klebsiella pneumoniae* pathogenic bacteria, utilizing an agar-well diffusion technique. The above bacteria were cultured in nutrient broth (NB) overnight at 37 °C. Each bacterium was adjusted to a 0.1 optical density at 600 nm (OD_{600}), and the bacteria were swabbed on nutrient agar (NA) plates using sterile cotton swabs. Five wells were bored into the NA agar using a sterile cork borer No.2 (6 mm diameter), and 100 µL of ZnONPs (100 mg/mL) were put into the wells. An antibiotic disc (streptomycin) was utilized as a positive control, and sterilized DI was the negative control. The NA plates were held for 1 h to complete diffusion. After that, the NA plates were incubated at 37 °C for 18 h. Finally, zones of inhibition (ZOI) were recorded.

2.5 Statistical analysis

The data were analyzed as mean ± standard error using the SPSS software. ZOI differences between morphologies were assessed using a one-way analysis of variance. Next, analysis of the differences in means of the samples with Duncan's multiple range tests ($P < 0.05$) was used.

3 Results and discussion

ZnONPs were synthesized using an aqueous solution of zinc acetate dehydrate (at a fixed concentration, 0.149 M) and NaOH in 4 different concentrations, 0.50, 0.72, 1.78, and 2.00 M. They were exposed to microwave radiation for 6 min at 800 W. The samples are referred to as ZnO-0.50 M NaOH, ZnO-0.72 M NaOH, ZnO-1.78 M NaOH, and ZnO-2.00 M NaOH, made with NaOH concentrations of 0.50, 0.72, 1.78, and 2.00 M, respectively. From visual observations, all the as-synthesized products were white colloidal solutions, as shown in the insets of Figure 1. The optical absorption properties of the synthesized products in Figure 1a were characterized using UV–vis spectroscopy over the 300–700 nm wavelength range. A strong absorption band was observed between 300 and 400 nm for all the samples, with clear absorption peaks at around 360 nm (3.44 eV) and 364 nm (3.41 eV), which corresponds to the absorption band of ZnO in the UV light region [42–45]. This absorption band is produced from the relaxation of excited electrons, which transition between the 3d-sp interband of ZnO [42]. The bandgap energy of ZnONPS was calculated using the Tauc plot method, as shown in Eq. (1).

$$(\alpha h\nu)^2 = A(h\nu - E_g) \quad (1)$$

where α is the absorption coefficient, h is Plank's constant, ν is photon frequency, A is the absorbance, and E_g is the band gap energy. The optical bandgap energies of ZnO-0.5 M NaOH, ZnO-0.72 M NaOH, ZnO-1.78 M NaOH, and ZnO-2.00 M NaOH were 3.20, 3.12, 3.04, and 3.08 electron volts (eV), respectively (Figure 1b). This indicates that as the particle size decreases, the bandgap of ZnONPs widens [46].

To extract information about the as-synthesized products, the surface morphology of the samples was further characterized to determine the influence of NaOH concentration on their morphologies. FESEM was used at a magnification of 50 kx. These results are shown in Figure 2 (on the left side). Four remarkably different ZnO nanostructure morphologies were observed. First, in Figure 2a at a NaOH concentration of 0.50 M, the ZnO-0.50 M NaOH sample presents morphology exhibiting uniformly distributed spherical and irregularly shaped particles of various sizes with little agglomeration and an approximate diameter of 46 nm (Figure 2c). Whereas at an NaOH concentration of 0.72 M, the ZnO-0.72 M NaOH sample (Figure 2d) shows flake-like ZnO nanostructures with an approximate diameter of 1.1 µm, consisting of nanosheet building blocks with thicknesses of about 53 nm (Figure 2f). By further increasing the NaOH concentration to 1.78 M, the ZnO-1.78 M NaOH sample, the morphology reveals flower-like ZnO nanostructures, shown in Figure 2g), which consist of a rod structure with an approximate diameter of 565 nm (Figure 2i). Last, morphology presented in Figure 2j of the ZnO-2.00 M NaOH sample shows rod-like ZnO nanostructures. The nanorods have various dimensions. Most of them show smooth surfaces forming perfect hexagonal rods with an approximate diameter of 490 nm (Figure 2l). From the FESEM results, it can be concluded that the sizes and morphologies of as-prepared ZnO powders depend markedly on the reactant concentration. However, the report by Proniewicz and colleagues, the stability of ZnONPs obtained by electrochemical dissolution of zinc was

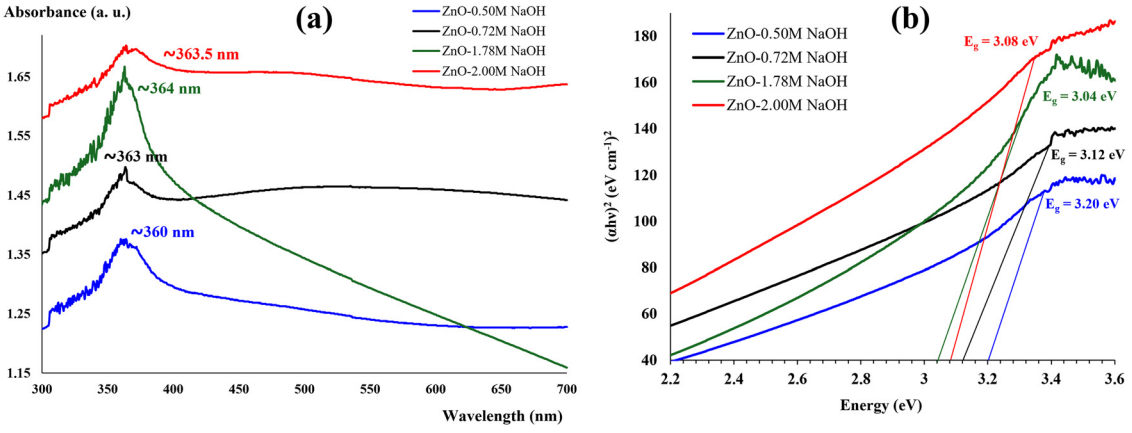

Figure 1: UV-visible spectrum (a) and band gap energy (b) of ZnO-0.5M NaOH, ZnO-0.72M NaOH, ZnO-1.78M NaOH, and ZnO-2.00M NaOH.

monitored immediately after synthesis and several times over the next 2 years by DLS analysis. It was found that the stability of ZnONP remained over time [42]. Figure 2 (on the middle) shows EDS analysis of all dried products to confirm the presence of ZnO nanostructures. The insets of Figure 2b, 2e, 2h, and 2k show the relative atom and weight ratio of oxygen (O), and zinc (Zn) for ZnO-0.50 M NaOH, ZnO-0.72 M NaOH, ZnO-1.78 M NaOH, and ZnO-2.00 M NaOH samples, respectively. According to the EDS results, the atomic percentages of Zn for ZnO-0.50 M NaOH, ZnO-0.72 M NaOH, ZnO-1.78 M NaOH, and ZnO-2.00 M NaOH were 46.80, 45.77, 66.81, and 48.25 %, respectively.

Next, the components and crystalline nature of the as-synthesized products were investigated using an XRD technique, with results shown in Figure 3. The XRD spectrum for each product exhibits sharp diffraction peaks at around 2θ = 31.87°, 34.51°, 36.35°, 47.61°, 56.69°, 62.93°, 66.40°, 68.19°, 69.12°, 72.50°, and 77.02°, attributed to the (100), (002), (101), (102), (110), (103), (200), (112), (201), (004), and (202) planes of ZnO nanostructures, respectively. Obtained values agreed

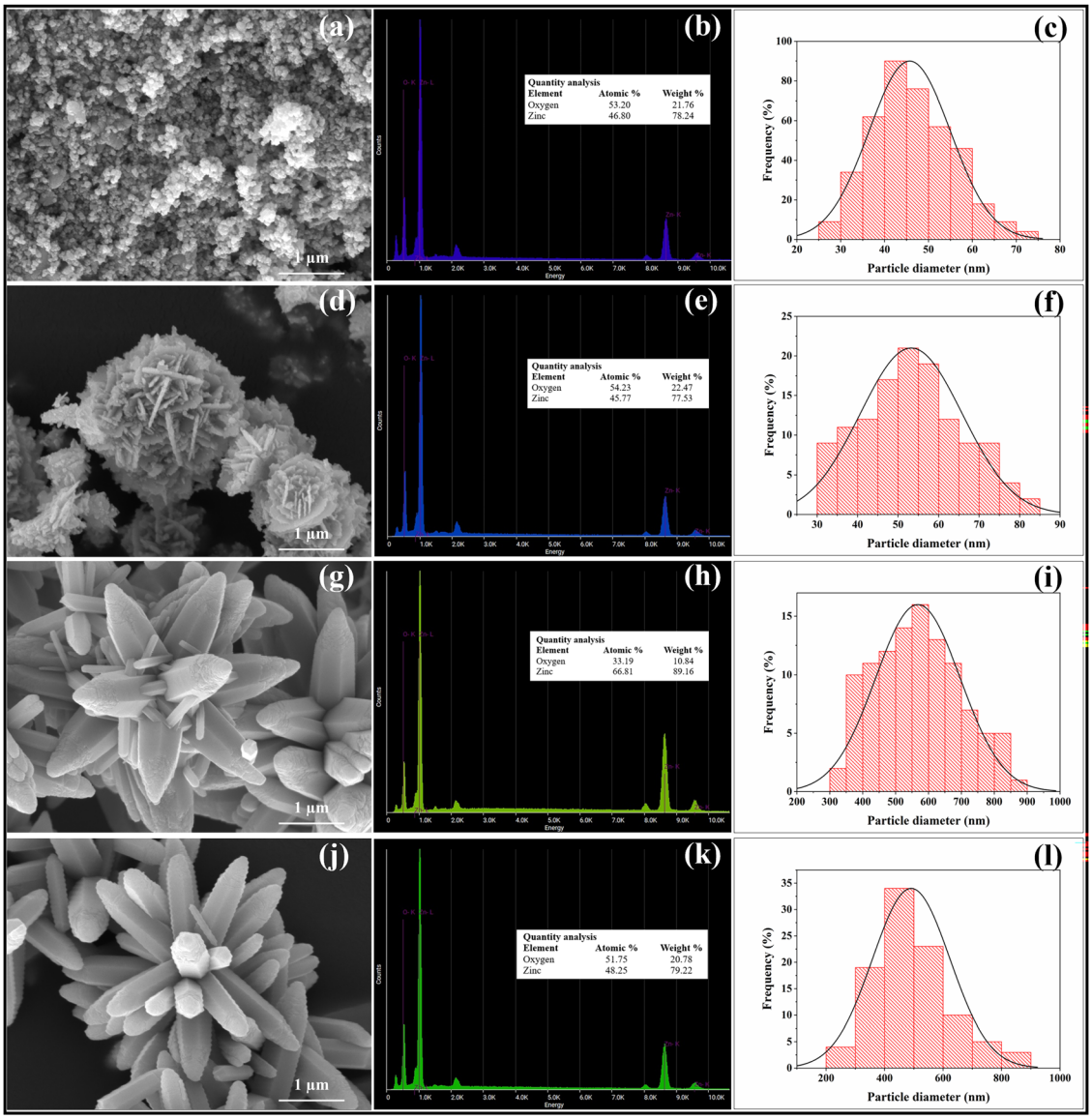

Figure 2: FESEM images (on the left side), EDX spectra were obtained from FESEM images (on the middle), and particle size distribution histograms (on the right side) of (a–c) ZnO-0.50 M NaOH, (d–f) ZnO-0.72 M NaOH, (g–i) ZnO-1.78 M NaOH, and (j–l) ZnO-2.00 M NaOH.

with those for previously reported ZnO nanostructures [42–45]. The XRD results confirm that each synthesized product with its various morphologies exhibited the typical single phase of the hexagonal wurtzite structure of ZnO material within the $P6_3mc$ space group indexed by the standard databases JCPDS card No. 751526 [45]. Additionally, no other diffraction peaks were observed in the spectrum of each sample. This suggests that the synthesized samples are highly pure wurtzite ZnO materials. The sharpness and intensity of peaks indicated that the products were well crystallized.

From the diffracted XRD peaks in Figure 3, the lattice parameters can be obtained from the following formula [42]:

$$\frac{1}{d_{hkl}^2} = \frac{4}{3}\left(\frac{h^2 + k^2 + hk}{a^2}\right) + \frac{l^2}{c^2} \quad (2)$$

The lattice parameters a, and c, in Eq. (2) can be calculated using the formulae $a = \frac{\lambda}{\sqrt{3}\sin\theta_{100}}$ and $c = \frac{\lambda}{\sin\theta_{002}}$, where λ is the X-ray radiation wavelength (1.5418 Å) employed, $\sin\theta_{100}$ and θ_{002} are the angles of diffraction peaks (100) and (002), respectively. Additionally, the h, k, and l indices of Eq. (2) indicate the crystal planes of the materials. Table 1 shows that the obtained "d_{hkl}" parameters are in good agreement with literature values [42, 43]. This suggests that the synthesized ZnONPs product has a crystalline form in a hexagonal wurtzite structure, according to the XRD results in Figure 3. Additionally, the unit cell volume for a hexagonal structure (V_{uc}) can be obtained using the formula $V_{uc} = \frac{3\sqrt{3}}{2}a^2c$ [42, 43]. The calculated lattice parameters are shown in Table 2.

FTIR measurements were performed over the wavenumber range from 400 cm^{-1} to 4,000 cm^{-1} to investigate molecular functional group adsorbing species on the surfaces of the as-synthesized samples and to detect molecular impurities. The obtained results reveal numerous absorption bands, shown in Figure 4. The solid (a), (b), (c), and (d) lines represent ZnO-0.50 M NaOH, ZnO-0.72 M NaOH, ZnO-1.78 M NaOH, and ZnO-2.00 M NaOH samples, respectively. From the FESEM images, as the concentration of NaOH was varied from 0.50 to 0.72 M, the morphology of the synthesized ZnONPs changed from a spherical shape (see FESEM image in Figure 2a) to a flake-like structure (Figure 2d). However, a slight change in the FTIR spectrum was observed (see solid line (a) and line (b) in Figure 4). They became flower and rod shapes of the synthesized ZnONPs as the NaOH concentration was increased to 1.78 and 2.00 M, changing the FTIR spectrum (see solid line (c) and line (d) in Figure 4), compared with the two previous spectra. In the

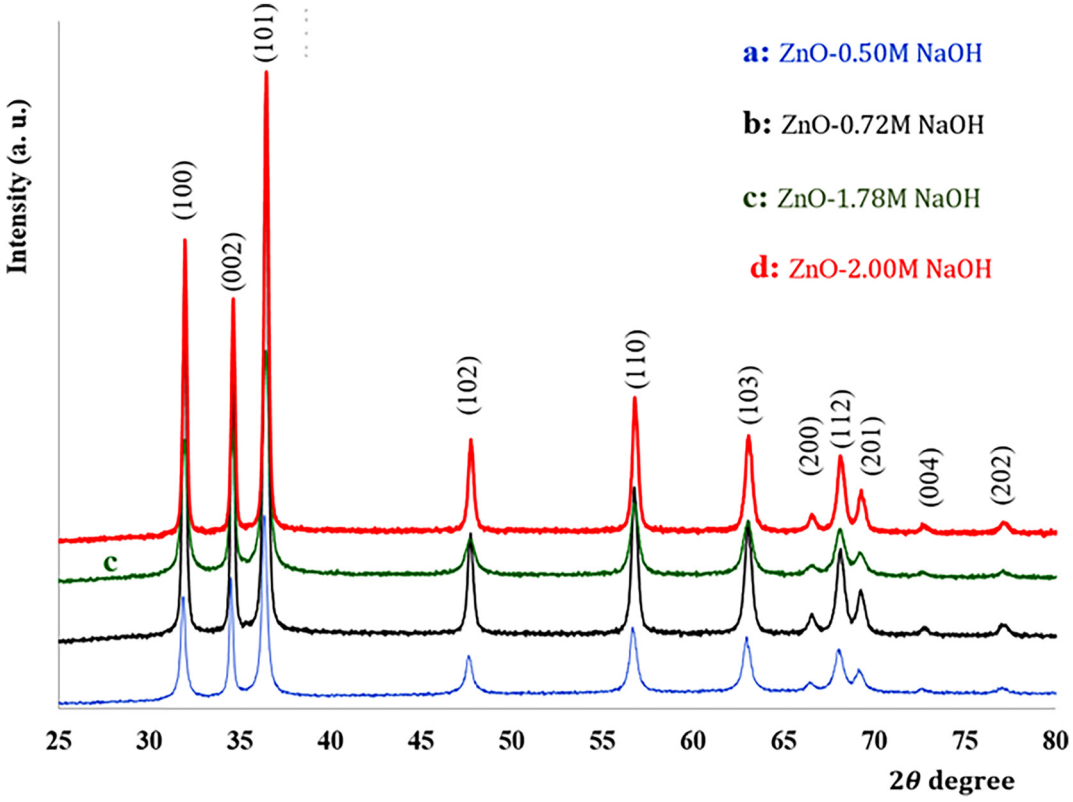

Figure 3: XRD patterns of the as-synthesized ZnO: (a) ZnO-0.50 M NaOH, (b) ZnO-0.72 M NaOH, (c) ZnO-1.78 M NaOH, and (d) ZnO-2.00 M NaOH.

Table 1: Interplanar spacing (d_{hkl}) from XRD compared with literature value [42] for corresponding (*hkl*)plane, percentage of variation of d_{hkl}.

hkl	2*θ* [degree]	d_{hkl} [Å] This work	d_{hkl} [Å] (Standard)
(100)	31.87	2.80	2.81
(002)	34.51	2.60	2.61
(101)	36.35	2.47	2.48
(102)	47.61	1.91	1.91
(110)	56.69	1.62	1.63
(103)	62.93	1.42	1.48
(200)	66.40	1.40	1.38
(112)	68.02	1.37	1.36
(201)	69.12	1.35	1.35

Table 2: Comparison between literature value and calculated unit cell parameters, cell volume, and $\frac{c}{a}$ ratio of ZnONPs obtained from XRD data [42].

Information	*a*[Å]	*c*[Å]	$\frac{c}{a}$	V_{uc} [Å^3]
This work	3.24	5.19	1.60	46.10
Standard	3.25	5.21	1.60	47.63

present investigations, the FTIR spectrum obtained from all samples shows an absorption peak centered at around 3,380 cm^{-1}, which can be attributed to the O–H stretching vibration mode. This may be due to the absorption of water in the solution during the mixing process by microwave radiation [47–49]. The other band peaks at around 1,336–1,640 cm^{-1} represent the stretching vibrations of the C=O mode [47–49]. The absorption band centered at 920–1,045 cm^{-1} is due to C–N stretching and C–H mode bending vibrations, respectively [47–49]. At lower concentrations of conditions of the reaction (0.50, 0.78 M) are used, reaction is not fully complete, and more acetate residues remain. The bands at 1,017 and 1,045 cm^{-1} are presented the C–O stretching [50]. In addition, at higher NaOH concentration conditions (1.78 and 2.0 M) appeared the band of 920 cm^{-1} which indicated the structural change or the formation of new surface species, and it associated with Zn–O–H bending confirms the formation of $Zn(OH)_2$, as the acetate is more removed [51]. The bands of 1,396 cm^{-1} and 1,636 cm^{-1} present C=O and C–H vibration due to the presence of partially transformed aldehyde or ketone groups are contributed from the zinc acetate as precursor [52]. At low wave numbers, the IR bands observed at approximately 446–677 cm^{-1} correspond to the stretching mode of ZnO nanostructures [53, 54]. Moreover, because during the synthesis of ZnONPs using alkaline solutions of NaOH, there is a possibility that zinc hydroxide ($Zn(OH)_2$) may be produced in the samples [53]. $Zn(OH)_2$ typically is formed when zinc ions (Zn^{2+}) react with hydroxide ions (OH^-). The results were presented in Figure 4. By identifying through FTIR

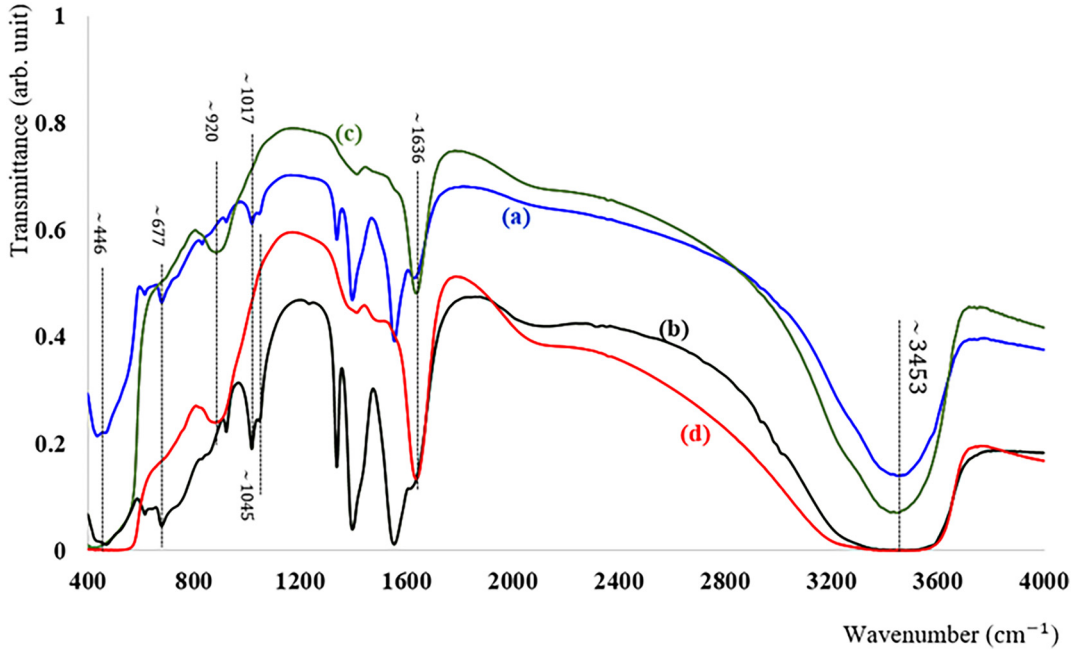

Figure 4: FTIR spectrum of the synthesized ZnONPs: Solid lines (a) were ZnO-0.50 M NaOH, (b) ZnO-0.72 M NaOH, (c) ZnO-1.78 M NaOH, and (d) ZnO-2.00 M NaOH.

spectroscopy, the compound exhibits broad O–H stretching bands (~3,400–3,500 cm^{-1}) from the hydroxyl groups, and Zn–OH related bands (~920 cm^{-1}) [55, 56]. In addition, XRD can also identify $Zn(OH)_2$ in the sample. As reported in Ref. [56, 57], diffraction peaks at 2θ = 32.8° and 33.5° correspond to $Zn(OH)_2$. However, the characteristic peaks of $Zn(OH)_2$ were not observed in this study, possibly because the $Zn(OH)_2$ content is below the detection limit of the XRD device. For Raman spectroscopy analysis, it cannot be sensitive enough to distinctly detect $Zn(OH)_2$, which can therefore be complemented with FTIR and XRD as mentioned above [56, 57].

The Raman scattering technique was utilized to clarify the quality and structure of the products. Hexagonal wurtzite ZnO belongs to the C_{6v}^4 space group with two formula units in the primitive cell. The vibrational modes of phonons at the Γ_{opt} point of the Brillouin zone were deduced from the following formula: $\Gamma_{opt} = A_1 + 2B_1 + E_1 + 2E_2$ [54, 58, 59], where the parameters A_1 and E_1 present polar modes and are both infrared and Raman active, while the mode B_1 is both infrared and Raman inactive (silent modes). The two non-polar E_2 modes ($E_{2L}$and E_{2H}, where L and H are denoted as low and high, respectively) are only Raman active. Additionally, modes A_1 and E_1 can be split into transverse (TO) and longitudinal optical (LO) phonons. The Raman spectra of the synthesized ZnO products were measured over a range of 300–700 cm^{-1}, and the corresponding results are illustrated in Figure 5.

Figure 5 shows the Raman spectra of ZnO-0.50 M NaOH, ZnO-0.72 M NaOH, ZnO-1.78 M NaOH, and ZnO-2.00 M NaOH samples. For all samples, a peak position, P_1, detected at around 330 cm^{-1} corresponds to E_{2H}-E_{2L}mode, which is recognized as a second order vibration mode occurring from the zone boundary phonon [54, 58]. A low intensity peak located at around 380 cm^{-1} (shown byP_2) is ascribed to the A_{1T}mode. The strongest peak, located at around 437 cm^{-1}, marked by P_3, is a characteristic mode E_{2H} for the hexagonal phase of ZnO, corresponding to oxygen vibration [54, 58]. The peak at around 583 cm^{-1}, shown by P_4 is ascribed to the E_{1L}mode, corresponding to second-order Raman scattering [58]. The peak positions of all synthesized products the details of vibration modes are summarized in Table 3, compared with theoretical value [59]. The experimental values show a clear shift in A_{1T} and E_{1L} modes, compared to the theoretical. The shifting of these modes is due to a combination of factors. First, it is possibly due to the defect engineering of ZnO. A partial presence of $Zn(OH)_2$, especially at high NaOH concentrations (see Figure 5), disturbs the ZnO crystal lattice, affecting the shift of the Raman-active modes

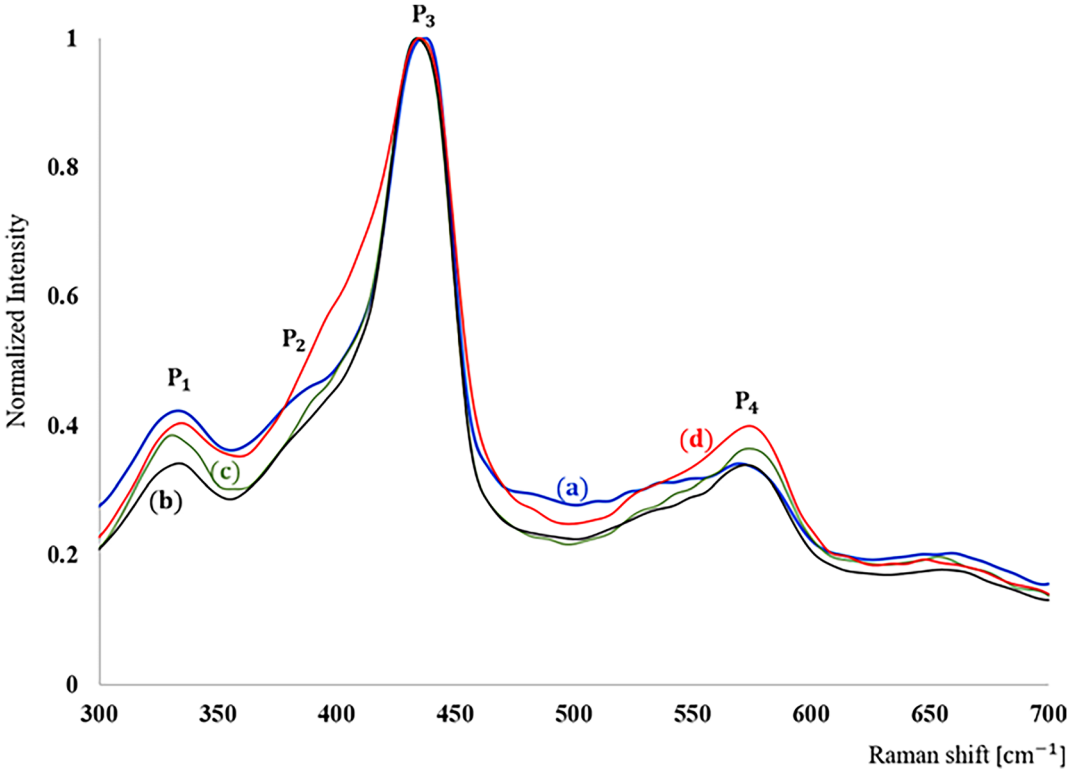

Figure 5: Raman spectra of the synthesized samples in the range 300–700 cm^{-1}: Solid lines (a) were ZnO-0.50 M NaOH, (b) ZnO-0.72 M NaOH, (c) ZnO-1.78 M NaOH, and (d) ZnO-2.00 M NaOH.

Table 3: Summary of the phonon mode frequencies of the synthesized samples compared with the theoretical results [59].

Peak no.	Assignment	Raman shift [cm^{-1}]				
		Theory [59]	Sample 1*	Sample 2*	Sample 3*	Sample 4*
P_1	E_{2H}-E_{2L}	333	335.99	333.44	329.26	335.99
P_2	A_{1T}	380	383.51	382.96	389.53	389.69
P_3	E_{2H}	437	438.42	436.43	436.43	436.43
P_4	E_{1L}	583	568.66	575.23	575.23	574.62

*Samples 1, 2, 3, and 4 denote ZnO-0.50 M NaOH, ZnO-0.72 M NaOH, ZnO-1.78 M NaOH, and ZnO-2.00 M NaOH, respectively.

[60]. The second factor is phonon confinement (size effect), proposed by Korepanov and coworkers [61]. As crystal size decreases, the vibrational coherence length shortens. And surface atoms, which have fewer neighboring atoms, vibrate differently from those in the bulk. These effects collectively contribute to phonon confinement, resulting in the shift of the Raman spectral peak as found in Figure 5.

Finally, the antimicrobial activity of the ZnO-0.50 M NaOH, ZnO-0.72 M NaOH, ZnO-1.78 M NaOH, and ZnO-2.00 M NaOH was tested against *E. coli*, *K. pneumoniae* (Gram-negative), *S. aureus*, and *B. subtilis* (Gram-positive) pathogenic bacteria using an agar-well diffusion method. The inhibition zones of all specimens are displayed in Figures 6 and 7. DI shows no ZOI. It was used as a negative control for all four bacterial strains. ZnO-0.50 M NaOH showed higher antimicrobial activity than other samples, with maximum ZOI diameters for *S. aureus* (20 ± 1.00 mm), *B. subtilis* (23.67 ± 2.31 mm), *E. coli* (17.33 ± 1.15 mm), and *K. pneumoniae* (12.83 ± 0.76 mm) as shown in Table 4. Our findings demonstrate that spherical-shaped ZnONPs manifest superior antibacterial efficacy when compared to flakes, flower, and rod morphologies. This might be attributed to the greater surface space and the smaller size of the spherical-shaped ZnONPs, which allows for better movement and passage through cell membranes, leading to greater antimicrobial activity [62]. However, ZnO-1.78 M NaOH has a flower-like morphology and is the largest in size, resulting in a low surface area, which results in low antibacterial activity. Additionally, the absence of core defects associated with zinc vacancies in the flower-like morphology results in a less efficient antibacterial effect. The existence of core defects associated with oxygen vacancies in all morphologies can damage bacterial cells' membranes with hydroxyl radicals, causing cell death [63]. Despite morphological differences, all morphological forms have antibacterial properties. Additionally, Zhang and colleagues report coupled recombinase polymerase amplification (RPA) with a lateral flow immunoassay (LFIA) readout system for *S. aureus* and *Vibrio parahaemolyticus* detection, showing great potential to address the on-site detection of foodborne pathogens in the future. Demonstrates the wide biomedical applications of nanomaterials [64]. Chandrasekaran and Pandurangan's report examined the cytotoxicity of ZnONPs against 3T3-L1 adipocytes and cocultured C2C12 myoblastoma cancer cells. The results indicated that ZnONPs caused a marked apoptosis and inhibited C2C12 cell proliferation more than 3T3-L1 cells. According to these findings, ZnONPs may be able to specifically trigger the death of cancer cells, making them a viable option for cancer treatment [65]. However, Elshafie and colleagues synthesize ZnO-NPs using chemical or green methods and investigate their antifungal activity against *Alternaria citri.* Results demonstrated that a concentration of 2,000 µg/mL was able to inhibit fungal growth by about 61 % (green ZnO-NPs) and 52 % (chemical ZnO-NPs). The results of this study showed that ZnONPs have high antifungal efficacy [66]. The antimicrobial efficacy of NPs may be based on their concentration, shape, size, and surface area among other factors [67, 68]. The produced ZnONPs have greater antimicrobial activity against Gram-positive bacteria than Gram-negative microorganisms. This phenomenon is possibly related to the structure of bacterial cell walls in interactions with ZnONPs. The ZnONPs bind to the exterior of the bacterial cell wall. Gram-positive bacterial cell walls have holes that allow ZnONPs to permeate. This results in internal leakage and cell death. Conversely, Gram-negative bacterial cell walls comprise phospholipids, lipopolysaccharides, and lipoproteins that function as a barrier to ZnONP penetration [69].

The antimicrobial mechanism of ZnONPs remains controversial and may be explained by several factors. One of the main factors affecting the antimicrobial activity is the release of zinc ions (Zn^{2+}). The released Zn^{2+} has the effect of inhibiting transport, disrupting amino acid metabolism, and affecting the enzyme system [70]. Pasquet et al. [71] revealed that the Zn^{2+} release mechanism is affected by the physicochemical properties of the ZnONPs, such as porosity, concentration, particle size, and morphology. In addition, Peng et al. [72] found that the morphology-dependent release of Zn^{2+} was observed, with the spherical structure exhibiting the greatest increase in Zn^{2+} release compared to the rod

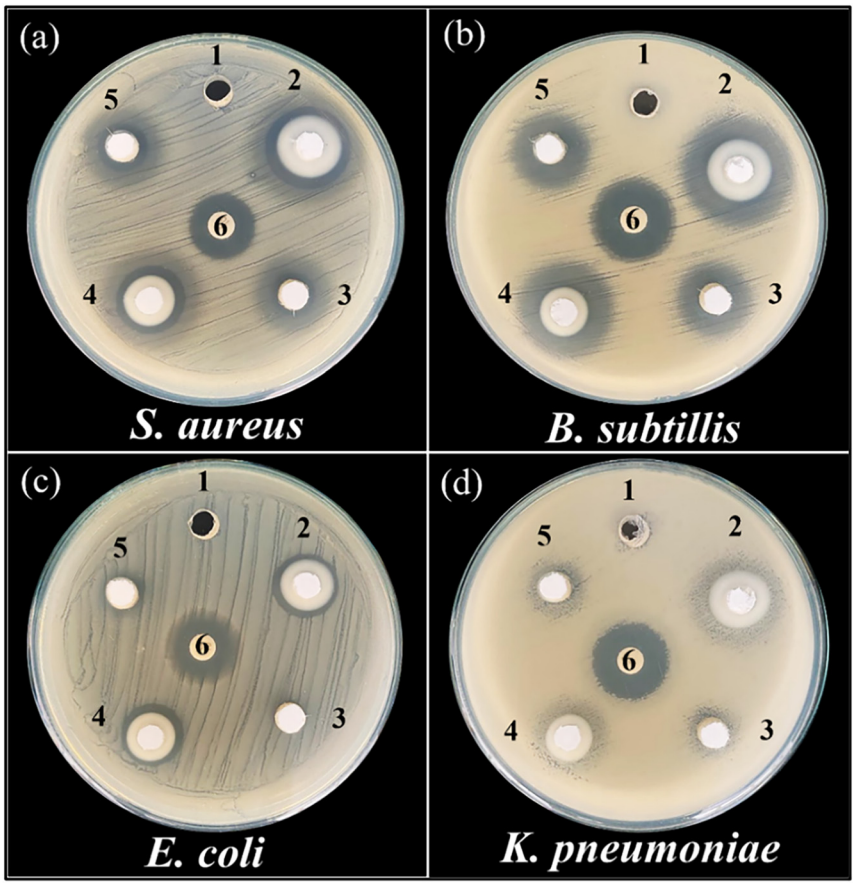

Figure 6: Antimicrobial activity of ZnONPs against (a) Staphylococcus aureus, (b) *B. subtillis*, (c) *Escherichia coli*, and (d) *Klebsiella pneumoniae* by agar well diffusion method. (1; DI, 2; ZnO-0.50 M NaOH, 3; ZnO-1.78 M NaOH, 4; ZnO-0.72 M NaOH, 5; ZnO-2.00 M NaOH, and 6; streptomycin).

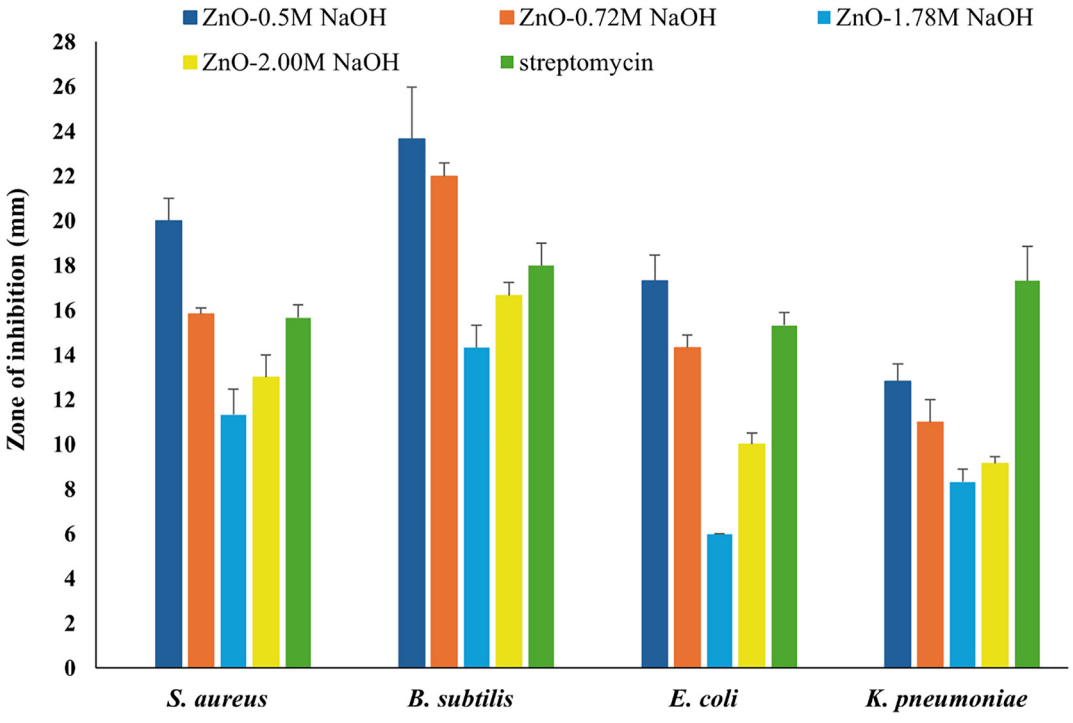

Figure 7: Comparison of the antimicrobial activity of ZnONPs against four pathogenic bacteria.

Table 4: Zone of inhibition (ZOI) values of different morphologies of ZnONPs against four pathogenic bacteria.

Sample	Zone of inhibition (mm) ± SD			
	Staphylococcus aureus	*Bacillus subtilis*	*Escherichia coli*	*Klebsiella pneumoniae*
ZnO-0.5 M NaOH	20.00 ± 1.00^{a}	23.67 ± 2.31^{a}	17.33 ± 1.15^{a}	12.83 ± 0.76^{a}
ZnO-0.72 M NaOH	15.83 ± 0.29^{b}	22.00 ± 0.58^{a}	14.33 ± 0.58^{b}	11.00 ± 1.00^{b}
ZnO-1.78 M NaOH	11.33 ± 1.15^{c}	14.33 ± 1.00^{b}	6.00 ± 0.00^{d}	8.33 ± 0.58^{c}
ZnO-2.00 M NaOH	13.00 ± 1.00^{c}	16.67 ± 0.58^{b}	10.00 ± 0.50^{c}	9.17 ± 0.29^{c}

Mean values with different superscripts in each row are significantly different by Duncan's multiple range test ($p < 0.05$).

structure. It has been explained that the curvature of the smaller surface of the spheres results in a higher solubility in equilibrium [72]. The release of Zn^{2+} attaches to the bacterial cell wall, leading to damage. Additionally, Zn^{2+} attacks DNA, causing damage and disrupting bacterial DNA replication, leading to bacterial death [73, 74]. The generation of reactive oxygen species (ROS) is the factor affecting the antibacterial activity of ZnONPs due to their high reactivity and oxidizing properties. Such reactive species are hydrogen peroxide (H_2O_2), hydroxyl radicals (OH^-), and superoxide anions ($\bullet O_2^-$) [75]. Electrons and holes react with water (H_2O) to produce •OH and H^+, while O_2 molecules form superoxide anions ($\bullet O_2^-$), which react with H^+ to produce $HO\bullet_2$. In addition, $HO\bullet_2$ disrupts electrons to form hydrogen peroxide ($\bullet HO_2$), which combines with H^+ to form hydrogen peroxide (H_2O_2) molecules [70]. The latter can penetrate cell membranes and may damage or kill bacteria. ROS reacts with proteins, enzymes, genetic materials, and other cellular elements, causing oxidative stress. The result is damage to bacteria and cell death [76].

4 Conclusions

In this study, ZnONPs with different morphologies were synthesized using a microwave-based process, with varying concentrations of NaOH. The synthesized ZnONPs were morphologically and structurally characterized using FESEM, EDX, FTIR, and XRD. The optical features of the ZnONPs were confirmed with UV–vis and Raman spectroscopy. The UV–vis spectra exhibit a prominent absorption band characteristic of ZnO. The diffraction peaks in the XRD pattern correspond to the (100), (002), (101), (102), (110), (103), (200), (112), (201), (004), and (202) planes of the ZnO hexagonal wurtzite structure. FTIR was confirmed by the presence of an absorption peak at 495-850 cm^{-1} corresponding to specific functional groups of ZnONPs. The synthesized ZnONPs with different morphologies show growth inhibition against Gram-positive *S. aureus* and *B. subtilis*, as well as Gram-negative *E. coli* and *K. pneumoniae*. According to the antimicrobial test results, ZnONPs of all morphologies can be used as antimicrobial agents. However, the current study is limited in its comprehensive efficacy testing *in vivo* and cytotoxicity tests. Further testing is needed in the future to investigate the efficacy of ZnONPs against multidrug-resistant bacteria and their mechanism of action.

Acknowledgments: We would like to thank you for the research on "Development of Zinc Oxide/Cotton Fabrics and Zinc Oxide/Bacterial Cellulose composite materials for Antimicrobial Activity" by Khon Kaen University received funding support from the National Science Research and Innovation Fund (NSRF). The authors thank all the researchers and laboratory members of the Biosafety Laboratory Level 2, Faculty of Interdisciplinary Studies, Khon Kaen University, for supporting their equipment, knowledge, and technical support.

Funding information: The research on "Development of Zinc Oxide/Cotton Fabrics and Zinc Oxide/Bacterial Cellulose composite materials for Antimicrobial Activity" by Khon Kaen University received funding support from the National Science Research and Innovation Fund (NSRF).

Author contributions: Wullapa Wongsinlatam: conceptualization, methodology, formal analysis, investigation, writing – original draft, and visualization; Jaruwan Thepsiri: formal analysis, investigation, methodology, writing – original draft, and visualization; Sasiporn Audtarat: formal analysis, investigation, methodology, writing – original draft, and visualization; Manop Sriuttha: formal analysis, investigation, and resources; Thananchai Dasri: conceptualization, methodology, writing – review and editing, supervision, project administration, and funding acquisition. All authors have accepted responsibility for the entire content of this manuscript and approved its submission.

Conflict of interest: The authors state no conflict of interest.

Data availability statement: All data generated or analysed during this study are included in this published article.

References

1. Altammar KA. A review on nanoparticles: characteristics, synthesis, applications, and challenges. Front Microbiol 2023;14:1155622.
2. Etemadi S, Mehravaran A, Delcheh EY, Khezri A, Nateghpour M, Haghi AM, et al. Green synthesis of PEGylated iron oxide nanoparticles of *Eriobotrya japonica* leaves extract in combination with B3, against *Plasmodium falciparum* 3D7 strain. Trop Med Health 2025;53:63.
3. Nikanjam S, Yeganegi A, Alikhani M-Y, Farmany A, Ghiasian SA, Hasanzade R. Novel antimicrobial applications of copper oxide nanoparticles after combination with tissue conditioner used in complete prostheses. BMC Oral Health 2024;24:752.
4. Soemphol C, Dasri T. Influence of silver nanoparticles on enhancing performance of optical absorption property in a perovskite solar cell. Nano Express 2024;5:035020.
5. Haji SH, Ganjo AR, Faraj TA, Fatah MH, Smail SB. The enhanced antibacterial and antibiofilm properties of titanium dioxide nanoparticles biosynthesized by multidrug-resistant *Pseudomonas aeruginosa*. BMC Microbiol 2024;24:379.
6. Chaisen K, Audtarat S, Thepsiri J, Dasri T. Development of antimicrobial cotton fabrics by decoration with silver nanoparticles and activated carbon composite. Mater Res Express 2023;10:105005.
7. Kovács K, Szierer A, Mészáros E, Molnár A, Rónavári A, Kónya Z, et al. Species-specific modulation of nitro-oxidative stress and root growth in monocots by silica nanoparticle pretreatment under copper oxide nanoparticle stress. BMC Plant Biol 2025;25:188.
8. Audtarat S, Thepsiri J, Chingsungnoen A, Dasri T. Ecofriendly surface improvement of cotton fabric by a plasma-assisted method to enhance silver nanoparticle adhesion for antimicrobial properties. Nanocomposites 2025;11:112–22.
9. Aggarwal R, Sheikh A, Akhtar M, Ghazwani M, Hani U, Sahebkar A, et al. Understanding gold nanoparticles and their attributes in ovarian cancer therapy. Mol Cancer 2025;24:88.
10. Unni V, Abishad P, Mohan B, Arya PR, Juliet S, John L, et al. Antibacterial and photocatalytic potential of piperine-derived zinc oxide nanoparticles against multi-drug-resistant non-typhoidal *Salmonella* spp. BMC Microbiol 2025;25:89.
11. Audtarat S, Wongsinlatam W, Thepsiri J, Dasri T. Fabrication of novel composite materials by impregnating ZnO particles into bacterial cellulose nanofibers for antimicrobial applications. Green Process Synth 2025;14:20250047.
12. Thepsiri J, Audtarat S, Dasri T. Green synthesis of silver nanoparticles using *Ageratum conyzoides* for activated carbon compositing to prepare antimicrobial cotton fabric. Nanotechnol Rev 2025;14:20250181.
13. Joudeh N, Linke D. Nanoparticle classification, physicochemical properties, characterization, and applications: a comprehensive review for biologists. J Nanobiotechnology 2022;20:262.
14. Sompech S, Jittabut P, Thaomola S, Audtarat S, Charee P, Dasri T. Localized surface plasmon resonance for improving optical absorption in core-shell Ag@TiO_2 nanoparticles. Sci Asia 2020;47:340–6.
15. Chen G, Wang Y, Xie R, Gong S. A review on core-shell structured unimolecular nanoparticles for biomedical applications. Adv Drug Deliv Rev 2018;130:58–72.
16. Dutta S, Chattopadhyay S, Sarkar A, Chakrabarti M, Sanyal D, Jana D. Role of defects in tailoring structural, electrical and optical properties of ZnO. Prog Mater Sci 2009;54:89–136.
17. Raha S, Ahmaruzzaman M. ZnO nanostructured materials and their potential applications: progress, challenges and perspectives. Nanoscale Adv 2022;4:1868–925.
18. Noshirvani N, Ghanbarzadeh B, Mokarram RR, Hashemi M. Novel active packaging based on carboxymethyl cellulose-chitosan-ZnO NPs nanocomposite for increasing the shelf life of bread. Food Packaging Shelf 2017;11:106–14.
19. Sultan M, Youssef A, Baseer RA. Fabrication of multifunctional ZnO@tannic acid nnanoparticles embedded in chitosan and polyvinyl alcohol blend packaging film. Sci Rep 2024;14:18533.
20. Sasidharan S, Tey L-H, Djearamane S, Rashid NKMA, Rajeshwari PA, Rajendran V, et al. Innovative use of chitosan/ZnO NPs bio-nanocomposites for sustainable antimicrobial food packaging of poultry meat. Food Packag Shelf Life 2024;43:101298.
21. Raj VJ, Ghosh R, Girigoswami A, Girigoswami K. Application of zinc oxide nanoflowers in environmental and biomedical science. BBA Advances 2022;2:100051.
22. Zhang H, Zhao X, Bai J, Tang M, Du W, Lv Z, et al. Effect of ZnO nanoparticle application on crop safety and soil environment: a case study of potato planting. Environ Sci Nano 2024;11:351–62.
23. Mendes CR, Dilarri G, Forsan CF, Sapata VMR, Lopes PRM, Moraes PB, et al. Antibacterial action and target mechanisms of zinc oxide nanoparticles against bacterial pathogens. Sci Rep 2022;12:2658.
24. Dey S, Mohanty DL, Divya N, Bakshi V, Mohanty A, Rath D, et al. A critical review on zinc oxide nanoparticles: synthesis, properties and biomedical applications. Intelligent Pharmacy 2025;3:53–70.
25. Wong YJ, Subramaniam H, Wong LS, Dhanapal ACTA, Chan YB, Aminuzzaman M, et al. Green synthesis and characterization of CuO/ZnO nanocomposite using *Musa acuminata* leaf extract for cytotoxic studies on colorectal cancer cells (HCC2998). Green Process Synth 2025;13:20240164.
26. Ahmad H, Siddique A, Zaheer S, Sattar R, Abbas A, Amin M, et al. Energy bandgap tuning of Sr-doped ZnO nanoparticles for photodegradation of azo dyes and antibacterial applications. JWPE 2025;24:107855.
27. Ullah S, Shaban M, Siddique AB, Zulfiqar A, Lali NS, Hassan MN, et al. Greenly synthesized zinc oxide nanoparticles: an efficient, cost-effective catalyst for dehydrogenation of formic acid and with improved antioxidant and phyto-toxic propertiesthe. J Environ Chem Eng 2024;12:113350.
28. Ghaffar S, Abbas A, Naeem-Ul-Hassan M, Assad N, Sher M, Ullah S, et al. Improved photocatalytic and antioxidant activity of olive fruit extract-mediated ZnO nanoparticles. Antioxidants (Basel) 2023;12:1201.
29. Chan YB, Aminuzzaman M, Win YF, Djearamane S, Wong LS, Guha SK, et al. *Garcinia mangostana* L. leaf-extract-assisted green synthesis of CuO, ZnO and CuO-ZnO nanomaterials for the photocatalytic degradation of palm oil mill effluent (POME). Catalysts 2024;14:486.
30. Chen Y-Y, Lee Y-H, Wang B-J, Chen R-J, Wang Y-J. Skin damage induced by zinc oxide nanoparticles combined with UVB is mediated by activating cell pyroptosis via the NLRP3 inflammasome–autophagy–exosomal pathway. Par Fibre Toxicol 2022;19:2.
31. Wibowo A, Marsudi MA, Amal MI, Ananda MB, Stephanie R, Ardy H, et al. ZnO nanostructured materials for emerging solar cell applications. RSC Adv 2020;10:42838–59.
32. Han Y, Guo J, Luo Q, Ma C-Q. Solution-processable zinc oxide for printed photovoltaics: progress, challenges, and prospect. Adv Energy Sustainability Res 2023;4:2200179.
33. Xie J, Cao Y, Jia D, Li Y, Wang Y. Solid-state synthesis of Y-doped ZnO nanoparticles with selective-detection gas-sensing performance. Ceram Int 2016;41:90–6.
34. Chan YB, Aminuzzaman M, Chuah X-T, Li K, Balu P, Wong LS, et al. Review in green synthesis mechanisms, application, and future prospects for *Garcinia mangostana* L. (mangosteen)-derived nanoparticles. Nanotechnol Rev 2025;14:20250157.

35. Chan YB, Aminuzzaman M, Rahman MK, Win YF, Sultana S, Cheah S-Y, et al. Green synthesis of ZnO nanoparticles using the mangosteen (*Garcinia mangostana* L.) leaf extract: comparative preliminary in vitro antibacterial study. Green Process Synth 2021;13:20230251.
36. Selvanathan V, Aminuzzaman M, Tan LX, Win YF, Cheah ESG, Heng MH, et al. Synthesis, characterization, and preliminary in vitro antibacterial evaluation of ZnO nanoparticles derived from soursop (*Annona muricata* L.) leaf extract as a green reducing agent. J Mater Res Technol 2022;20:2931–41.
37. Ismillayli N, Suprapto S, Santoso E, Nugraha RE, Holilah H, Bahruji H, et al. Microwave-assisted synthesis of silver nanoparticles as a colorimetric sensor for hydrogen peroxide. RSC Adv 2024;14:6815–22.
38. Darakai V, Punsawad C, Jitonnom J, Nisoa M, Rattanakit P. Microwave-assisted ultrafine silver nanoparticle synthesis using *Mitragyna speciosa* for antimalarial applications. Green Process Synth 2024;13:20230257.
39. Gao Y, Wang Y, Jiang J, Wei P, Sun H. Triggered "On/off" luminescent polypeptide bowl-shaped nanoparticles for selective lighting of tumor cells. Small 2025;21:e2411432.
40. Gao C, Sun H, Du J. Unusual endotaxy growth of hexagonal nanosheets by the self-assembly of a homopolymer. Angew Chem Int Ed 2025;64: e202420079.
41. Abbas A, Mansoor S, Nawaz MH, Chaudhry AA, Ijaz K, Riaz S, et al. Growth of diazonium-functionalized ZnO nanoflakes on flexible carbon cloth for electrochemical sensing of acetone in the liquid phase. RSC Adv 2023;17:11537–45.
42. Proniewicz E, Tata A, Wojcik A, Starowicz M, Pacek J, Molenda M. SERS activity and spectroscopic properties of Zn and ZnO nanostructures obtained by electrochemical and green chemistry methods for applications in biology and medicine. Phys Chem Chem Phys 2020;22:28100–14.
43. Raoufi D. Synthesis and photoluminescence characterization of ZnO nanoparticles. J Lumin 2013;134:213–19.
44. Perillo PM, Atia MN, Rodríguez DF. Effect of the reaction conditions on the formation of the ZnO nanostructures. Physica E 2017;85:185–92.
45. Das A, Nair RG. Effect of aspect ratio on photocatalytic performance of hexagonal ZnO nanorods. J Alloys Compd 2020;817:153277.
46. Gherbi B, Laouini SE, Meneceur S, Bouafia A, Hemmami H, Tedjani ML, et al. Effect of pH value on the bandgap energy and particles size for biosynthesis of ZnO nanoparticles: efficiency for photocatalytic adsorption of methyl orange. Sustainability 2022;14:11300.
47. Bhardwaj R, Bharti A, Singh JP, Chae KH, Goyal N, Gautam S. Structural and electronic investigation of ZnO nanostructures synthesized under different environments. Heliyon 2018;4:e00594.
48. Maensiri S, Laokul P, Promarak V. Synthesis and optical properties of nanocrystalline ZnO powders by a simple method using zinc acetate dihydrate and poly (vinyl pyrrolidone). J Cryst Growth 2006;289:102–6.
49. Bousslama W, Elhouichet H, Gelloz B, Sieber B, Addad A, Moreau M, et al. Structural and luminescence properties of highly crystalline ZnO nanoparticles prepared by sol-gel method. Jpn J Appl Phys 2012;51: 04DG13.
50. Murthy KRS, Raghu GK, Binnal P. Zinc oxide nanostructured material for sensor application. J Adv Biotechnol Bioeng 2021;5:25–9.
51. Zakirov MI, Semen'ko MP, Korotchenkov OA. A simple sonochemical synthesis of nanosized ZnO from zinc acetate and sodium hydroxide. J Nano Electron Phys 2018;10:05023.
52. Thongam DD, Gupta J, Sahu NK. Effect of induced defects on the properties of ZnO nanocrystals: surfactant role and spectroscopic analysis. SN Appl Sci 2019;1:1030.
53. Das R, Kumar A, Kuma Y, Sen S, Shirage PM. Effect of growth temperature on the optical properties of ZnO nanostructures grown by simple hydrothermal method. RSC Adv 2015;5:60365–72.
54. Kumar Y, Rana AK, Bhojane P, Pusty M, Bagwe V, Sen S, et al. Controlling of ZnO nanostructures by solute concentration and its effect on growth, structural and optical properties. Mater Res Express 2015;2: 105017.
55. Faheem M, Siddiqi HM, Habib A, Shahid M, Afzal A. ZnO/$Zn(OH)_2$ nanoparticles and self-cleaning coatings for the photocatalytic degradation of organic pollutants. Front Environ Sci 2022;10:965925.
56. Winiarski J, Tylus W, Winiarska K, Szczygieł I, Szczygieł B. XPS and FT-IR characterization of selected synthetic corrosion products of zinc expected in neutral environment containing chloride ions. J Spectrosc. 2018:2079278.
57. Emara MM, Ragab DM, Kassem TSE. Deposition of ZnS dots onto nanosheets of cobalt-doped ZnO-$Zn(OH)_2$ and their photocatalytic activity. J Phys Chem Solids 2021;148:109702.
58. Casamassa E, Fioravanti A, Mazzocchi M, Carotta C, Faga MG. Abrasive properties of ZnO: influence of different nanoforms. Tribol Int 2020; 142:105984.
59. Song Y, Zhang S, Zhang C, Yang Y, Lv K. Raman spectra and microstructure of zinc oxide irradiated with swift heavy ion. Crystals 2019;9:395.
60. Gurylev V, Perng TP. Defect engineering of ZnO: review on oxygen and zinc vacancies. J Eur Ceram Soc 2021;41:4977–96.
61. Korepanov VI, Chan S-Y, Hsu H-C, Hamaguchi H-O. Phonon confinement and size effect in raman spectra of ZnO nanoparticles. Heliyon 2019;5:e01222.
62. Siddiqi KS, Ur Rahman A, Tajuddin HA. Properties of zinc oxide nanoparticles and their activity against microbes. Nanoscale Res Lett 2018;13:141.
63. Talebian N, Amininezhad SM, Doudi M. Controllable synthesis of ZnO nanoparticles and their morphology-dependent antibacterial and optical properties. J Photochem Photobiol B 2013;120:66–73.
64. Zhang Y, LiuDual X, Luo J, Liu H, Li Y, Liu J, et al. Recombinase polymerase amplification system combined with lateral flow immunoassay for simultaneous detection of *Staphylococcus aureus* and *Vibrio parahaemolyticus*. J Pharm Biomed Anal 2025;255:116621.
65. Chandrasekaran M, Pandurangan M. In vitro selective anti-proliferative effect of zinc oxide nanoparticles against co-cultured C2C12 myoblastoma cancer and 3T3-L1 normal cells. Biol Trace Elem Res 2016;172:148–54.
66. Elshafie HS, Osman A, El-Saber MM, Camele I, Abbas E. Antifungal activity of green and chemically synthesized ZnO nanoparticles against *Alternaria citri*, the causal agent citrus black rot. Plant Pathol J 2023;39: 265–74.
67. Islam KS, Mustak MH, Shishir MKH, Karim MM, Khan GMA. Biosynthesis of ZnO nanoparticles using banana peel pectin for antibacterial and photocatalytic applications. S Afr J Chem Eng 2025;52:127–40.
68. Shi L-E, Li Z-H, Zheng W, Zhao Y-F, Jin Y-F, Tang Z-X. Synthesis, antibacterial activity, antibacterial mechanism and food applications of ZnO nanoparticles: a review. Food Addit Contam: Part A 2014;31: 173–86.
69. Tran XT, Bien TTL, Tran TV, Nguyen TTT. Biosynthesis of ZnO nanoparticles using aqueous extracts of *Eclipta prostrata* and *Piper longum*: characterization and assessment of their antioxidant, antibacterial, and photocatalytic properties. Nanoscale Adv 2024;6:4885–99.
70. Sirelkhatim A, Mahmud S, Seeni A, Kaus NHM, Ann LC, Bakhori SKM, et al. Review on zinc oxide nanoparticles: antibacterial activity and toxicity mechanism. Nano-Micro Lett 2015;7:219–42.
71. Pasquet J, Chevalier Y, Pelletier J, Couval E, Bouvier D, Bolzinger M-A. The contribution of zinc ions to the antimicrobial activity of zinc oxide. Colloids Surf A 2014;457:263–74.

72. Peng X, Palma S, Fisher NS, Wong SS. Effect of morphology of ZnO nanostructures on their toxicity to marine algae. Aquat Toxicol 2011; 102:186–96.
73. Kalra K, Chhabra V, Prasad N. Antibacterial activities of zinc oxide nanoparticles: a mini review. J Phys Conf Ser 2022; 2267: 012049.
74. Kumar R, Umar A, Kumar G, Nalwa HS. Antimicrobial properties of ZnO nanomaterials: a review. Ceram Int 2017;43:3940–61.
75. Cao YH, Cai WJ, He XW, Song H-L, Gao J, Yang Y-L, et al. A review of advances & potential of applying nanomaterials for biofilm inhibition. NPJ Clean Water 2024;7:131.
76. Klink MJ, Laloo N, Taka AL, Pakade VE, Monapathi ME, Modise JS. Synthesis, characterization and antimicrobial activity of zinc oxide nanoparticles against selected waterborne bacterial and yeast pathogens. Molecules 2022;27:3532.